



PCCP

**A Combined Experimental and Computational Study on the
 $\tilde{A}_{1}^2 A^{\prime} / \tilde{A}_{2}^2 A^{\prime \prime} - \tilde{X}^2 A^{\prime}$ Transition of the Calcium
 Isopropoxide Radical as a Candidate for Direct Laser Cooling**

Journal:	<i>Physical Chemistry Chemical Physics</i>
Manuscript ID	CP-ART-09-2021-004107.R2
Article Type:	Paper
Date Submitted by the Author:	02-Mar-2022
Complete List of Authors:	Telfah, Hamzeh; University of Louisville , Department of Chemistry Sharma, Ketan; The Ohio State University, Department of Chemistry Paul, Anam; University of Louisville , Department of Chemistry Riyadh, S. M. Shah; University of Louisville , Department of Physics and Astronomy Miller, Terry; The Ohio State University, Department of Chemistry Liu, Jinjun; University of Louisville , Department of Chemistry; University of Louisville , Department of Physics and Astronomy

SCHOLARONE™
 Manuscripts

A Combined Experimental and Computational Study on the $\tilde{A}_1^2A'/\tilde{A}_2^2A'' - \tilde{X}^2A'$ Transition of the Calcium Isopropoxide Radical as a Candidate for Direct Laser Cooling

Hamzeh Telfah,^{1,†} Ketan Sharma,² Anam C. Paul,^{1,‡} S. M. Shah Riyadh,³ Terry A. Miller² and Jinjun Liu^{1,3,}*

1. Department of Chemistry, University of Louisville, Louisville, Kentucky 40292, United States
2. Department of Chemistry, the Ohio State University, Columbus, Ohio 43210, United States
3. Department of Physics and Astronomy, University of Louisville, Louisville, Kentucky 40292, United States

* Corresponding Author. E-mail: j.liu@louisville.edu.

[†] Current address: Department of Mechanical and Aerospace Engineering, the Ohio State University, Columbus, OH 43210, USA.

[‡] Current address: Veeco Instruments, Inc., San Jose, CA 95134, USA.

Abstract

Vibronically resolved laser-induced fluorescence/dispersed fluorescence (LIF/DF) and cavity ring-down (CRD) spectra of the $\tilde{A}_1^2A'/\tilde{A}_2^2A'' - \tilde{X}^2A'$ electronic transition of the calcium isopropoxide $[\text{CaOCH}(\text{CH}_3)_2]$ radical have been obtained under jet-cooled conditions. An essentially constant $\tilde{A}_2 - \tilde{A}_1$ energy separation of 68 cm^{-1} has been observed for the vibrational ground levels and all fundamental vibrational levels accessed in the LIF measurement. To simulate the experimental spectra and assign the recorded vibronic bands, Franck-Condon (FC) factors and vibrational branching ratios (VBRs) are predicted from vibrational modes and their frequencies calculated using the complete-active-space self-consistent field (CASSCF) and equation-of-motion coupled-cluster singles and doubles (EOM-CCSD) methods. Combined with the calculated $\tilde{A}_1/\tilde{A}_2 - \tilde{X}$ electronic transition energy, the computational results, especially those from the EOM-CCSD calculations, reproduced the experimental spectra with considerable accuracy. The experimental and computational results suggest that the FC matrix for the studied electronic transition is largely diagonal, but transitions from the vibrationless levels of the \tilde{A} state to the \tilde{X} -state levels of the CCC bending (ν_{14} and ν_{15}), CaO stretch (ν_{13}), and CaOC asymmetric stretch (ν_9 and ν_{11}) modes also have considerable intensities. Transitions to low-frequency in-plane [ν_{17} (a')] and out-of-plane [ν_{30} (a'')] CaOC bending modes were observed in the experimental LIF/DF spectra, the latter being FC-forbidden but induced by the pseudo-Jahn-Teller (pJT) effect. Both bending modes are coupled to the CaOC asymmetric stretch mode *via* the Duschinsky rotation, as demonstrated in the $\tilde{A}_1^2A'/\tilde{A}_2^2A'' \rightarrow \tilde{X}^2A'$ DF spectra obtained by pumping non-origin vibronic transitions. The pJT interaction also induces transitions to the ground-state vibrational level of the ν_{10} (a') mode, which has the CaOC bending character. Our

combined experimental and computational results provide critical information for future direct laser cooling of the target molecule and other alkaline earth monoalkoxide radicals.

Keywords: laser cooling molecules, Franck-Condon factors, vibrational branching ratios, pseudo-Jahn-Teller effect, spin-orbit, Duschinsky rotation, laser-induced fluorescence, dispersed fluorescence, cavity ring-down.

1. Introduction

Alkaline earth monoalkoxide free radicals (MORs) are promising candidates for direct laser cooling to sub-millikelvin temperatures.¹⁻³ The calcium methoxide radical, CaOCH_3 , is the first nonlinear molecule that has been laser-cooled.⁴ CaOCH_3 , as well as other alkaline earth monomethoxides, is a symmetric top and belongs to the C_{3v} point group. Early work on its spectroscopy was done by the Bernath group.^{5,6} Its ground electronic state is a 2A_1 state, while its first excited state is a 2E state, although the latter is split into two spin-orbit (SO) components (the lower-energy $^2E_{1/2}$ and the higher-energy $^2E_{3/2}$). The 2E state, being orbitally doubly degenerate, is also subject to the Jahn-Teller (JT) effect.^{7,8} Furthermore, the \tilde{A}^2E state is coupled to the neighboring \tilde{B}^2A_1 state *via* the pseudo-Jahn-Teller (pJT) effect.⁵ These spin-vibronic interactions affect not only the vibronic structure of the lowest electronic states of the CaOCH_3 radical,⁹⁻¹¹ but also its rotational and fine structure.¹¹⁻¹⁵

Recently, the possibility of direct laser-cooling asymmetric tops,^{1-3, 16} including complex organic molecules,¹⁷⁻²¹ has been explored. Such molecules will have broad applications in cold chemistry,²²⁻²⁶ quantum information and quantum computing,^{27, 28} fundamental physics,²⁹⁻³⁸ and other related fields.^{39, 40} Due to the lowered symmetry, the analysis of the spin-vibronic structure of asymmetric-top molecules subject to the pJT and SO effects is a challenging task.^{41, 42} Similarly, the rotational and fine structure of asymmetric tops in nearly degenerate electronic states can also be intimidatingly intricate.^{43, 44} As a spectroscopic preparation for future laser cooling of asymmetric tops, our group recorded laser-induced fluorescence/dispersed fluorescence (LIF/DF) and cavity ring-down (CRD) spectra of the $\tilde{A}_1^2A''/\tilde{A}_2^2A' - \tilde{X}^2A'$ electronic transition of the calcium ethoxide (CaOC_2H_5) radicals under the jet-cooled

conditions.⁴² Aided by complete-active-space self-consistent-field (CASSCF) and coupled-cluster (CC) calculations with the inclusion of vibronic and SO coupling, we were able to reproduce the spin-vibronic structure of experimentally obtained $\tilde{A}_1^2A''/\tilde{A}_2^2A' \leftrightarrow \tilde{X}^2A'$ spectra of CaOC_2H_5 . Moreover, the vibrational branching ratios (VBRs) were also determined in our experiment, a critical piece of information for future laser cooling of this free radical.¹⁶

Calcium ethoxide can be regarded as the single methyl substitution of calcium methoxide. It is interesting to compare the calcium ethoxide results to calcium isopropoxide, $\text{CaOCH}(\text{CH}_3)_2$, the double methyl substitution. Such a comparison resembles our previous work on ethoxy and isopropoxy radicals,⁴⁵⁻⁴⁷ although, for asymmetric-top alkoxy radicals, it is the ground (\tilde{X}) and the first excited (\tilde{A}) states that are nearly degenerate. Going from ethoxy to isopropoxy, symmetries of the two lowest electronic states are interchanged. Upon alkyl substitution, the upper ($\tilde{X}^2E_{1/2}$) and lower ($\tilde{X}^2E_{3/2}$) SO components of the methoxy radical are coupled by the zero-point-energy (ZPE)-corrected “difference potential”^{43-46, 48-61} between the A' and A'' states $\Delta E_0 = E(A') - E(A'')$. (See Ref. [43] for detailed discussion on spin-vibronic coupling between two nearly degenerate electronic states.) ΔE_0 may take positive or negative values, leading to the A'' or A' state as the lower state, respectively. For instance, the ground electronic state of ethoxy, originating from the $\tilde{X}^2E_{3/2}$ state of methoxy, is dominantly a $^2A''$ state, whereas that of the isopropoxy is dominantly a $^2A'$ state. For alkoxy radicals, such a change in symmetry-related energy order is attributed to the interactions of the methyl groups and the half-filled $p\pi$ orbital.^{45, 46, 58} (See Section III of Ref. [46] for detailed discussion and quantum chemistry calculations of the $^2A' - ^2A''$ separations of ethoxy and isopropoxy.) In addition, the SO interaction coupling the A' and A'' states diminishes dramatically going from ethoxy (-71 cm^{-1}) to isopropoxy (-39 cm^{-1}).⁴⁶

In the same fashion, one might expect that the symmetries of the \tilde{A}_1 and \tilde{A}_2 states of calcium ethoxide and calcium isopropoxide are exchanged too. (The \tilde{A}_1 and \tilde{A}_2 states, respectively, are the lower- and higher-energy electronic states that originate from the \tilde{A}^2E state of calcium methoxide.) Similar to the \tilde{X} state of ethoxy, the \tilde{A}_1 state of calcium ethoxide is expected to have the A'' symmetry, while that of the calcium isopropoxide, like the \tilde{X} state of isopropoxy, be an A' state. Both the experimental and computational results from our previous work⁴² on CaOC_2H_5 and the present work on $\text{CaOCH}(\text{CH}_3)_2$ (see below) confirm the expected symmetries. Furthermore, the vibrational structures of both the \tilde{X} and \tilde{A}_1/\tilde{A}_2 states are also expected to be different for the two radicals. A generalized spectroscopy model and the detailed analysis of symmetries and coupling between nearly degenerate $^2A'$ and $^2A''$ states, as well as the effect of such coupling on the spin-ro-vibronic structure and spectra, can be found in our previous publications.^{42, 43, 46, 58}

In the present work, we report the LIF/DF and CRD spectra of jet-cooled $\text{CaOCH}(\text{CH}_3)_2$ radicals and spectral simulations based on quantum chemistry calculations. The experimental setup used in the present work is identical to those reported in our previous work on CaOCH_3 and CaOC_2H_5 .^{10, 42} The only change in the present experiment is that the organic precursor used in the present work is isopropanol. Therefore, experimental details are given in the Supporting Information (SI).

2. Quantum Chemistry Calculations and Spectral Simulation

In the present paper, we simulate the experimental spectra using computational results on the CASSCF(3,6)/cc-pVTZ and EOMEA-CCSD/cc-pVTZ levels of theory. For the CASSCF calculations, the molecular orbitals included in the active space are the $3p_z$, $4s$, $3d_z$, $4p_x$, $4p_y$, and $5s$ orbitals of the Ca atom, although the $5s$ orbital is strongly mixed with the $4p_z$ orbital of Ca. (See Figure 1.) An attempt was made to include the $4p_z$ orbital of calcium into the active space, but the geometry optimization at the conical intersection failed to converge. Following our previous publications, the C_s symmetry plane is defined as the zx plane in the molecule-fixed frame, with the z -axis oriented toward the OCa bond. The y axis is perpendicular to the C_s plane. The energy calculations confirmed the $\tilde{A}_1^2A'/\tilde{A}_2^2A''$ symmetries for the lowest excited states of $\text{CaOCH}(\text{CH}_3)_2$. Because the \tilde{A}_1 and \tilde{A}_2 states are nearly degenerate, the state-averaged (SA) CASSCF method was adopted for geometry optimization. Therefore, the \tilde{A} -state geometry reported here (see Table 1) is the optimized minimum of the conical intersection seam and therefore is the same for both states.

The second set of electronic structure calculations presented here was done using the CFOUR suite.⁶² The geometries of the \tilde{X} , \tilde{A}_1 and \tilde{A}_2 states were optimized individually using the Equation-of-Motion Electron Affinity Coupled-Cluster Singles and Doubles (EOMEA-CCSD) method with correlation-consistent triple zeta (cc-pVTZ) basis set. The reference state for the EOMEA-CCSD calculations is the ground state of the cation of $\text{CaOCH}(\text{CH}_3)_2$. These calculations provide the equilibrium bond lengths and bond angles for the three electronic states as well as the rotational constants, as summarized in Table 1. Further, harmonic vibrational frequencies were also calculated at the EOMEA-CCSD/cc-pVTZ level using finite differentiation of analytic gradients.

Equilibrium bond lengths and bond angles, as well as rotational constants, of both the \tilde{X} and \tilde{A} states, are summarized in Table 1. The largest change in the bond length upon the $\tilde{A}_1/\tilde{A}_2 \leftarrow \tilde{X}$ excitation is in the contraction of the CaO bond. ($\Delta r_{\text{CaO}} \sim 25$ and 3.1 pm according to the CASSCF and EOM-CCSD calculations, respectively.) Therefore, one expects vibronic transitions to the CaO stretch levels in the LIF/DF spectra to be significant.

CASSCF and EOM-CCSD calculations also provided the vibrational frequencies and modes of both the \tilde{X} and \tilde{A} states. Calcium isopropoxide has 17 a' modes and 13 a'' modes. The \tilde{X} - and \tilde{A} -state frequencies of these modes are given in Table 2. Franck-Condon factors (FCFs) for both absorption and emission transitions under the harmonic oscillator approximation were calculated using ezSpectrum^{63, 64} (for CASSCF results) and FCSquared⁶⁵ (for EOM-CCSD results) with the inclusion of Duschinsky rotation.⁶⁶ The transition frequencies and intensities were then used to generate the simulated $\tilde{A}_1/\tilde{A}_2 \leftarrow \tilde{X}$ LIF spectrum and the $\tilde{A}_1/\tilde{A}_2 \rightarrow \tilde{X}$ DF spectrum using a home-built program. The simulated spectra are compared with experimental ones in Figures 2 and 3. In simulating the LIF spectrum, the vibrational temperature is set to 50 K. The Gaussian line shape with a full-width at half-maximum (FWHM) of 5 cm^{-1} and 25 cm^{-1} was used to generate the simulated LIF and DF spectra, respectively

Simulations reported in the present paper are based on the Born-Oppenheimer (BO) and the harmonic-oscillator approximations. It is well known that the non-BO vibronic interactions (e.g., the JT and pJT effects) and the SO interaction can alter the spin-vibronic structure of degenerate and nearly degenerate electronic states and introduce transitions that are otherwise forbidden. The vibronic interactions can be treated in the effective-Hamiltonian approach originally developed by Köppel, Domcke, and Cederbaum (KDC).⁶⁷ The KDC model has been applied to

study the vibronic structure and simulate the experimental spectra of various molecules in coupled electronic states (see, for example, Refs. [68-70] and references therein), notably, the NO_3 radical.⁷¹⁻⁷⁵ The SO interaction has also been incorporated in the effective Hamiltonian to investigate spin-vibronic structure of degenerate or nearly degenerate states of free radicals.^{8, 76, 77} In our previous work on the calcium methoxide¹⁰ and ethoxide⁴² radicals, a spin-vibronic Hamiltonian was constructed using the quasi-diabatic basis that involves the \tilde{A} and \tilde{B} states. Experimentally recorded LIF and DF spectra of both radicals have been reproduced using the spin-vibronic Hamiltonian. Due to its relative large size and number of vibrational modes, such multi-state multi-mode spin-vibronic treatment of calcium isopropoxide is not feasible at this stage, limited by computational capabilities. (See Section 3.3 for details.) Nevertheless, signatures of spin-vibronic interaction have been revealed in the LIF and DF spectra of calcium isopropoxide. Especially, transitions that would have vanishing or extremely small intensities have been observed in the experimental spectra, which is attributed to vibronic interactions. (Vide infra.)

3. Results

3.1. Laser-Induced Fluorescence (LIF) Spectrum

The experimentally recorded $\tilde{A}_1/\tilde{A}_2 \leftarrow \tilde{X}$ LIF spectrum is illustrated in Figure 2a in comparison with the simulations using results from the EOM-CCSD and CASSCF calculations (Figures 2b and 2c). The experimental spectrum consists of seven doublets separated by $\sim 68 \text{ cm}^{-1}$, which is attributed to both the SO splitting and the ZPE-corrected difference potential (ΔE_0) between the A' and A'' states, with the latter probably mostly due to BO interactions and to a lesser extent by

non-BO interactions, i.e., pJT effects. Previously, it has been experimentally determined that the $\tilde{A}^2\Pi_{3/2} - \tilde{A}^2\Pi_{1/2}$ separation of calcium monohydroxide [66.8181(12) cm^{-1}],⁷⁸ the $\tilde{A}^2E_{3/2} - \tilde{A}^2E_{1/2}$ separation of calcium methoxide [66.97448(51) cm^{-1}],¹³ and the $\tilde{A}_2^2A' - \tilde{A}_1^2A''$ separation of calcium ethoxide^{42, 79} are all close to 67 cm^{-1} . For calcium ethoxide, the SO splitting ($a\zeta_e d = 62 \text{ cm}^{-1}$) and the ZPE-corrected difference potential (i.e., the SO-free separation, $\Delta E_0 = 17 \text{ cm}^{-1}$) have been predicted independently in CC calculations⁴², with the former being the dominant contribution to the overall $\tilde{A}_2 - \tilde{A}_1$ separation:

$$\Delta E^{\tilde{A}_2 - \tilde{A}_1} = \sqrt{(a\zeta_e d)^2 + (\Delta E_0)^2} \quad (1)$$

For calcium isopropoxide, a $\Delta E^{\tilde{A}_2 - \tilde{A}_1}$ value of 68 cm^{-1} is determined in its LIF spectra, while the EOM-CCSD calculations predicted that $\Delta E_0 = 34 \text{ cm}^{-1}$. Combining these two values, the SO constant $a\zeta_e d$ is calculated as 59 cm^{-1} . Obtaining more precise values for $a\zeta_e d$ and ΔE_0 of calcium ethoxide and isopropoxide relies on future rotationally resolved LIF spectra. (See Discussion in Ref. [42].) Nevertheless, the current and previous results on CaOR radicals suggest that the alkyl substitution does not affect the SO splitting significantly. Table 3 summarizes, wherever available, the calculated and experimentally determined $a\zeta_e d$, ΔE_0 , and $\Delta E^{\tilde{A}_2 - \tilde{A}_1}$ values for calcium methoxide, ethoxide, and isopropoxid radicals.

The strongest doublet centered at $\sim 15844 \text{ cm}^{-1}$ is assigned to the origin transition, with the lower- and higher-frequency peaks assigned to the $\tilde{A}_1^2A' \leftarrow \tilde{X}^2A'$ (15810 cm^{-1}) and the $\tilde{A}_2^2A'' \leftarrow \tilde{X}^2A'$ (15878 cm^{-1}) transitions, respectively. The experimental origin frequency should be compared to the EOM-CCSD-calculated value of 16060 cm^{-1} and the CASSCF-calculated value of 15452 cm^{-1} . In our previous work on calcium methoxide and ethoxide radicals, the EOM-CCSD

calculations predicted the $\tilde{A} \leftarrow \tilde{X}$ excitation energy with high accuracy: 15918 cm^{-1} (cal'd) v.s. 15925 cm^{-1} (expt.) for calcium methoxide¹⁰ and 15869 cm^{-1} (cal'd) v.s. 15882 cm^{-1} (expt.) for calcium ethoxide.⁴² The relative errors of the predicted values are less than 0.1% for these two free radicals. However, it is significantly larger (1.3%) for the calcium isopropoxide radical. Experimental and calculated $\Delta E^{\tilde{A} \leftarrow \tilde{X}}$ values of calcium methoxide, ethoxide, and isopropoxide radicals are summarized in Table 3. It is worth noting that the calculated electronic transition frequencies (T_e 's in Tables 1 and 3) do not contain the ZPE corrections. Under the harmonic-oscillator approximation and using the EOM-CCSD-calculated harmonic frequencies, the ZPEs of the \tilde{A}_1 and \tilde{A}_2 states of calcium isopropoxide are 28 and 48 cm^{-1} larger than its \tilde{X} state, respectively. Although anharmonicity, especially that due to the pJT-active modes, may modify the ZPE differences between the \tilde{A}_1/\tilde{A}_2 and the \tilde{X} states, it is not sufficient to explain the discrepancy between the experimental and calculated $\tilde{A}_1/\tilde{A}_2 - \tilde{X}$ electronic transition energies (216 cm^{-1}). Similarly, the changes to the $\tilde{A}_1/\tilde{A}_2 - \tilde{X}$ electronic transition frequencies of calcium methoxide and ethoxide radicals due to the ZPE correction are negligible compared to their absolute values. Therefore, the extremely small discrepancies between the experimental and EOM-CCSD-calculated $\tilde{A} \leftarrow \tilde{X}$ transition frequencies of calcium methoxide and ethoxide may be fortuitous. CASSCF calculations systematically underestimated the $\tilde{A} \leftarrow \tilde{X}$ transition frequencies of calcium methoxide [15359 cm^{-1} (cal'd) v.s. 15925 cm^{-1} (expt.)], ethoxide [15390 cm^{-1} (cal'd) v.s. 15882 cm^{-1} (expt.)], and isopropoxide [15452 cm^{-1} (cal'd) v.s. 15844 cm^{-1} (expt.)]. An averaged scaling factor of 1.031(6) may be applied to the CASSCF-calculated origin frequency to match the experimental value.

By comparing the experimental LIF spectrum to vibronic transition frequencies and intensities

simulated using results from the EOM-CCSD calculations (Figure 2b), doublets centered at 318, 443, 556, and 842 cm^{-1} to the blue of the origin band can be assigned to transitions to the \tilde{A}_1/\tilde{A}_2 ($v^{\prime}=1$) levels of the ν_{15} , ν_{14} , ν_{13} , and ν_{12} modes, respectively. (See Table 2 and Figure 2.) The ν_{15} , ν_{14} , and ν_{13} modes all have the character of CaOC bending in the C_s symmetry plane. Modes ν_{15} and ν_{14} are dominated by CCC bending, i.e., the change of the dihedral angle between the two OCC planes. The phases between the CaOC and the CCC bendings are opposite for ν_{15} and ν_{14} . Mode ν_{13} is the CaO stretch mode. The transitions to the CaO stretch levels are weaker than the transitions to the two CCC bending modes, which has been predicted by the EOM-CCSD calculations. The ν_{12} mode (842 cm^{-1}) is the symmetric stretch-motion of the two CC bonds.

The EOM-CCSD calculations better predict the vibronic spectrum than CASSCF in terms of both vibrational frequencies and transition intensities. For instance, in the simulation based on CASSCF calculations (Figure 2c), the transition to the CaO stretch level (ν_{13}) is stronger than the transitions to the two CCC bending modes (ν_{15} and ν_{14}), which is contradictory to the experimental observation. In the higher-frequency region ($>1000 \text{ cm}^{-1}$), the CASSCF simulation failed to predict the dominant feature of the 12_0^1 transition. Instead, it predicted two strong combination transitions in this region, $13_0^1 15_0^1$ and $13_0^1 16_0^1$ along with the 12_0^1 transition.

The weaker two doublets with smaller blue shifts from the origin (centered at 83 and 101 cm^{-1}) are assigned to transitions to the \tilde{A} -state levels of the out-of-plane [$\nu_{30}(a'')$] and in-plane [$\nu_{17}(a')$] CaOC bending modes, respectively. The CASSCF calculations predict vibrational frequencies of 102 cm^{-1} and 126 cm^{-1} for the out-of-plane and the in-plane modes, respectively. Again, the EOM-CCSD calculations provide more accurate vibrational frequencies for the ν_{30} level: 87 cm^{-1} . For the ν_{17} level, the EOM-CCSD calculations provided different vibrational

frequencies for the two excited states: 104 and 110 cm^{-1} for the \tilde{A}_1^2A' and \tilde{A}_2^2A'' states, respectively. (See Table 2.)

In this low-frequency region, there are three major discrepancies between the experimental and predicted transition intensities. First, transitions to the $\nu_{30} = 1$ (a'') levels are forbidden under the BO approximation because the FCF vanishes for symmetry reasons. Therefore, neither the CASSCF nor EOM-CCSD simulations predict the 30_0^1 transition. However, in the experimental LIF spectrum, transitions to the $\nu_{30} = 1$ levels have considerable intensities (with $\text{FCF}=0.051$, see Table 4). Second, the EOM-CCSD calculations predict a small FCF for the 17_0^1 band (an averaged value of 0.0048 for the two SO components), while the 17_0^1 FCF predicted by the CASSCF calculations is diminishingly small. In the experimental LIF spectrum, the 17_0^1 band has a transition intensity that is almost identical to the 30_0^1 band. Finally, for the 17_0^1 band, the EOM-CCSD calculations predict significantly different FCFs for the $\tilde{A}_1^2A' \leftarrow \tilde{X}^2A'$ and $\tilde{A}_2^2A'' \leftarrow \tilde{X}^2A'$ transitions: 0.0078 and 0.0018, respectively. (See Figure 2 and Table 4.) This is not unexpected given that the CaOC bond angle of the \tilde{A}_1^2A' state (178.0° according to the EOM-CCSD calculations) is quite different from the \tilde{X}^2A' state (178.4°), whereas that of the \tilde{A}_2^2A'' state (178.5°) is much closer to the \tilde{X}^2A' state. (See Table 1.) However, in the experimental IIF spectrum, the two transitions have similar intensities. (See Figure 2a.)

It is important to stress that the current simulations do not include the vibronic coupling, i.e., the pJT effect (see Section 3.3 for more details), which explains discrepancies between the experimentally obtained and calculated transition intensities. In calcium isopropoxide, the $\nu_{30}(a'')$ mode couples the A' and A'' states, reduces the symmetry of their potential energy surfaces (PESs), and, hence, is responsible for forming the conical intersection. The $\nu_{17}(a')$ mode reduces

the energy gap between the A' and A'' states. (The a'' and a' modes are, therefore, referred to by KDC as the “coupling mode” and the “tuning mode”, respectively.^{41, 67}) The pJT interaction mixes the $\nu=0$ level (the vibrational ground level) of the A' state with the fundamental ($\nu=1$) levels of the bending modes of the A'' state, and vice versa. As a result, the transitions to the $\nu=1$ levels borrow intensities from the origin transition and become allowed.^{10, 42, 46} (See, for example, Figure 7 of Refs. [10].) The fact that the transitions to the $\nu_{17}(a')$ and $\nu_{30}(a'')$ vibronic levels are of comparable and considerable intensities suggests that the pJT interaction between the A' and A'' states is strong for $\text{CaOCH}(\text{CH}_3)_2$, which shall be tested in future vibronic analysis. Moreover, the observation that transitions to the $\nu_{17}=1$ levels of the A' and A'' states have similar intensities is attributed to strong quadratic vibronic interaction that couples the two SO components.⁸ In our previous spin-vibronic calculations of CaOCH_3 , a strong quadratic JT interaction was predicted.¹⁰ Therefore, it is reasonable to expect that a strong quadratic interaction is present in the \tilde{A} -state $\text{CaOCH}(\text{CH}_3)_2$ as well.

A broader peak ($\Delta\nu \sim 10 \text{ cm}^{-1}$) was observed at 188 cm^{-1} . Based on the DF spectrum obtained by pumping this band, it is assigned to the transition to the $\nu'=2$ levels of the $\nu_{30}(a'')$ mode. (See Section 3.2.) The fundamental frequency of the \tilde{A} -state ν_{30} mode is 83 cm^{-1} . (See above.) Therefore, the 30^2 level has an anharmonicity that increases the vibrational energy from twice the fundamental frequency. The broadening can be attributed to an unresolved SO splitting, which is significantly smaller than the 68 cm^{-1} separations of \tilde{A} -state fundamental levels. Both the anomalous anharmonicity and the unusually small SO splitting are not unexpected. The ν_{30} mode is a pJT-active mode, and the PES along this mode is highly anharmonic. (See, for example, previous experimental and computational investigation of PESs of the nearly degenerate \tilde{X} and \tilde{A} states of alkoxy radicals belonging to the C_s point group.^{46, 58, 80-85})

Rotationally resolved LIF spectra and a detailed spin-vibronic analysis similar to previous work on the $\text{CaOH } \tilde{A}^2\Pi(020) - \tilde{X}^2\Sigma^+(000)$ band⁸⁶ and our work on the calcium ethoxide radical⁴² are required to determine and model the energy level structure in the low-energy region.

The CASSCF calculations predict a strong transition to the vibrational levels of in-phase double-methyl rotation (ν_{16}) at 286 cm^{-1} . (See Figure 2c.) Transition intensities for the 16_0^1 band predicted in the EOM-CCSD calculations are significantly smaller: FCF=0.0027 for the $\tilde{A}_1^2A' \leftarrow \tilde{X}^2A'$ transition and 0.0021 for the $\tilde{A}_2^2A'' \leftarrow \tilde{X}^2A'$ transition. The reason for the strong 16_0^1 transitions in the CASSCF-based simulation is that the CASSCF calculations predict a large methyl rotation from the \tilde{X} state to the \tilde{A} state. The fact that such a transition was not recorded in the experimental LIF spectrum (Figure 2a) suggests the absence of a considerable methyl rotation upon the electronic excitation. Note that the barriers for the methyl rotation in $\text{CaOCH}(\text{CH}_3)_2$ are relatively low, which reduces the precision of geometry optimization along the methyl-rotation dimensions. Nevertheless, the EOM-CCSD calculations provided a more reliable prediction of the transition intensities to the double-methyl rotation levels.

3.2. Dispersed Fluorescence (DF) Spectra

Figures 3a and 3c illustrate DF spectra obtained by pumping the $\tilde{A}_1^2A' \leftarrow \tilde{X}^2A'$ and $\tilde{A}_2^2A'' \leftarrow \tilde{X}^2A'$ origin transitions of $\text{CaOCH}(\text{CH}_3)_2$, respectively. Except for transitions due to collision-induced population transfer between the \tilde{A}_1 and \tilde{A}_2 states (asterisked in the figures)^{10, 42, 79} the two DF spectra are almost identical. Similar to the LIF spectrum, strong peaks at 312, 432, and 543 cm^{-1} in the DF spectra are assigned to transitions to the $\nu'' = 1$ levels of the ν_{15} (CCC

bending), ν_{14} (CCC bending), and ν_{13} (CaO stretch) modes, respectively. Like in the LIF spectrum, the transition to the ν_{15} level is the strongest of off-diagonal transitions. The EOM-CCSD calculations predicted both vibrational frequencies and transition intensities with better accuracies than the CASSCF calculations. (See Figures 3b, 3d, and 3e and Tables 2 and 4.)

Above 1000 cm^{-1} red-shift, three peaks are observed at 1015, 1100, and 1181 cm^{-1} . The EOM-CCSD calculations predict three fundamental vibrational levels in this region: ν_{11} (at 1063 cm^{-1}), ν_{10} (1203 cm^{-1}), and ν_9 (1257 cm^{-1}), respectively. (See Figures 3b, 3d, and 3e and Table 2.) Therefore, we assign the peaks at 1015, 1100, and 1181 cm^{-1} to transitions to the $\nu''=1$ levels of ν_{11} , ν_{10} , and ν_9 , respectively, although the EOM-CCSD calculations did not provide an accurate prediction of their relative intensities. The EOM-CCSD calculations predicted relative intensities for the 11_1^0 and 9_1^0 transitions comparable to the experimental observations. (See experimental and calculated FCFs in Table 4.) However, the EOM-CCSD-calculated FCF for the 10_1^0 transition is vanishingly small [FCF(10_1^0) $\sim 10^{-4}$]. Both the $\nu_{11}(a')$ and $\nu_9(a')$ modes are CaOC asymmetric stretch (CaO and OC bonds stretching out-of-phase) combined with the umbrella motion of the two methyl groups and the hydrogen atom that is connected to the central carbon atom. These two modes differ in the phase between the CaOC stretch and the umbrella motions. The $\nu_{10}(a')$ mode possesses an in-plane CaOC bending character. (See Figure S.1 for the ν_{10} mode.) Therefore, like $\nu_{17}(a')$, ν_{10} is also a pJT “tuning mode”, and the 10_1^0 transition gains intensity from the vibronic interaction between the \tilde{A}_1^2A' and \tilde{A}_2^2A'' states. The CASSCF calculations predict the three vibrational levels at $\nu_{11}=1127 \text{ cm}^{-1}$, $\nu_{10}=1278 \text{ cm}^{-1}$, and $\nu_9=1327 \text{ cm}^{-1}$, significantly less accurately than the EOM-CCSD calculations. (See Figure 3e.)

Finally, the weak peak at 96 cm^{-1} red-shift in the $\tilde{A}_1^2A' \rightarrow \tilde{X}^2A'$ DF spectrum is assigned to the

transition to the $v''=1$ level of the in-plane CaOC bending mode [ν_{17} (a')]. The EOM-CCSD calculations predict a harmonic frequency of 105 cm^{-1} for this pJT-related mode, and the predicted transition intensity is comparable to the experimental value ($\text{FCF}_{\text{cal'd}}=0.007$ v.s. $\text{FCF}_{\text{expt}}=0.012$.) In the $\tilde{A}_2^2A'' \rightarrow \tilde{X}^2A'$ DF spectrum, this peak is obscured by the strong $\tilde{A}_1^2A' \rightarrow \tilde{X}^2A'$ origin band following the $\tilde{A}_2^2A'' \rightarrow \tilde{A}_1^2A'$ population transfer (asterisked in Figure 3c). The EOM-CCSD-predicted FCF for the $\tilde{A}_2^2A'' \rightarrow \tilde{X}^2A'$ 17_1^0 transition is 0.002, 3.5 times weaker than that for the $\tilde{A}_1^2A' \rightarrow \tilde{X}^2A'$ 17_1^0 transition. However, like in the LIF spectrum, the two SO components of the 17_1^0 transition have similar intensity due to the pJT mixing. (See discussion in Section 3.1.) The CASSCF calculations predict that the ground-state frequency of ν_{17} is 120 cm^{-1} , but the predicted intensity of the transition to this level is vanishingly small. (See Figure 3e.)

The ground-state frequency of the out-of-plane CaOC bending mode [ν_{30} (a'')] is predicted by the CASSCF calculations to be 95 cm^{-1} , i.e., 25 cm^{-1} to the red of the in-plane one [ν_{17} (a')]. The EOM-CCSD calculations predict a ground-state frequency of 85 cm^{-1} for this mode, 20 cm^{-1} red-shifted from ν_{17} . It is, therefore, possible that the pJT-induced, relatively weaker 30_1^0 transition is obscured by the relatively strong 17_1^0 transition due to the limited resolution of the DF spectra ($\sim 25\text{ cm}^{-1}$). If this is the case, the two transitions may be resolved in future DF measurements with better resolution or stimulated-emission pumping (SEP) measurements.⁸⁷

Similar to the LIF spectrum (Section 3.1), the CASSCF calculations predict a strong 16_1^0 transition at 298 cm^{-1} , where ν_{16} is the in-phase double methyl rotation, whereas the EOM-CCSD calculations predicted a significantly smaller intensity for this transition. This transition was not observed in the DF spectra for the reasons stated above. (See Section 3.1.)

Transitions to the \tilde{X}^2A' -state ν_{12} level (symmetric CC stretch) are predicted with considerable intensities (FCF=0.003) in both CASSCF and EOM-CCSD calculations. (See Figures 3b, 3d, and 3e.) The CASSCF and EOM-CCSD-calculated frequencies for ν_{12} are 893 and 870 cm^{-1} , respectively. However, these transitions were not observed in the DF spectra. Both CASSCF and EOM-CCSD calculations predict a contraction of the CC bonds by 0.2 pm upon the $\tilde{A}_1^2A'/\tilde{A}_2^2A'' \leftarrow \tilde{X}^2A'$ excitation (Table 1), which explains the predicted 12_1^0 transition intensities. The absence of the 12_1^0 transitions in the DF spectra suggests that the CC bond change may be significantly smaller than calculated.

When other vibronic transitions to the \tilde{A} -state fundamental levels, namely, 30_0^1 , 17_0^1 , 15_0^1 , 14_0^1 and 13_0^1 , are pumped, the strong bands in the DF spectra include the origin band and the transition to the fundamental vibrational level of the pumped mode in the \tilde{X}^2A' ground electronic state due to favorable FCFs. (See Figures 4b-c, 4e-g.) In addition, when the 15_0^1 transition in the LIF spectrum is pumped, the $\tilde{A}_1^2A'/\tilde{A}_2^2A'' \rightarrow \tilde{X}^2A'$ transition to the first overtone of the ν_{15} mode (CCC bending+CaOC bending) is also observed at 629 cm^{-1} . (See Figure 4e.) The DF spectra pumping the 12_0^1 (842 cm^{-1}) have also been recorded, but no peak other than the origin band was observed.

When transitions to the \tilde{A} -state levels of the two bending modes (17_0^1 and 30_0^1) are pumped, a fluorescence band to the 10_1 level at 1100 cm^{-1} is also observed. (See Figures 4b and 4c.) This is expected because of the in-plane CaOC bending character of the ν_{10} mode. (See Figure S.1.)

The DF spectrum obtained by pumping the LIF band at 188 cm^{-1} (Figure 4d) deserves special comments. In addition to the origin band, this DF spectrum contains a strong peak, whose red-

shift is close to the expected transition to the 13_130_1 combination level. (In Figure S.2. This spectrum is illustrated in full scale, which demonstrates the large intensity of this band.) This DF band also appears when the 30_0^1 transition in the LIF spectrum is pumped (see Figure 4b), although the intensity there is significantly smaller. Both observations suggest Duschinsky mixing between ν_{13} and ν_{30} modes. The three weaker transitions in the DF spectrum pumping the 188 cm^{-1} LIF band can be assigned to the 30_1^0 (81 cm^{-1}), $13_1^030_2^0$ (687 cm^{-1}), and $13_2^030_4^0$ (1325 cm^{-1}) transitions. The 188 cm^{-1} LIF band is, therefore, assigned to the 30_0^2 transitions, although detailed experimental and computational studies are required to confirm this assignment. (See Section 3.1.)

3.3. Limitations and Possible Extensions of the Current Simulations

The CASSCF calculations reported in the present work underestimate the electronic transition frequency by $\sim 3\%$ and overestimate the vibrational frequencies by $\sim 12\%$. This is attributed to the lack of dynamic correlation effects in the CASSCF method.^{88, 89} The EOM-CCSD calculations do a much better job at predicting the vibrational frequencies of the various modes, overestimating them by $\sim 4\%$. A full spin-vibronic treatment^{10, 42} of $\text{CaOCH}(\text{CH}_3)_2$ is certainly desirable, and we believe that such a calculation likely will provide a much more accurate simulation of the vibronic spectra as in our previous work on CaOCH_3 and CaOC_2H_5 . Further, such a calculation will provide quantitative insight into the SO and pJT interactions present in the molecule. We believe that these interactions play a very important role in explaining some of the spectral features observed in the experiments and such a simulation would also help up in reproducing the fine structure in the experimental spectra.

However, at this point, it is not possible for us to do a complete spin-vibronic treatment for the calcium isopropoxide radical due to computational limitations. To give an estimate, we would be required to diagonalize a spin-vibronic matrix that would have to include at least 8 vibrational modes and 3 electronic states (\tilde{A}_1 , \tilde{A}_2 , and \tilde{B}), which all lie within approx. 3000 cm^{-1} of each other. This would require diagonalizing matrices with more than 600 million basis functions (even if we separate the a' and a'' modes and ignore any couplings between the modes of different symmetries), which is much greater than the current computational capability of our spin-vibronic program,^{8, 74, 90} namely, SOCJT3. We are presently working to extend SOCJT3 to be able to handle such huge matrices.

While quantitative prediction of all the features of the observed spectra is not yet possible, it is possible to rationalize the principal discrepancies between the observed spectra and the current simulations. For example, the predicted FCF for 17_0^1 from the EOM-CCSD calculation is only about 16% of the experimentally observed value. In addition, the 30_0^1 and 30_0^2 bands (out-of-plane bending) are observed in the LIF spectra with significant intensity, while neither CASSCF nor EOM-CCSD calculations predict any significant intensity in either band. Indeed, in the absence of the pJT and SO coupling, the 30_0^1 transition would be forbidden by symmetry as ν_{30} is an a'' mode. Qualitatively, these two modes are similar to the two components of the ν_8 bending mode of CaOCH_3 ,¹⁰ which is both JT and pJT active. Based on its values in CaOCH_3 , pJT and SO coupling will allow intensity in transitions to the ν_{30} mode by mixing the A' and A'' states, and it is likely strong given the quite small A' and A'' splitting predicted by the electronic EOM-CCSD calculation (34 cm^{-1}). It is expected that the corresponding two modes in $\text{CaOCH}(\text{CH}_3)_2$ (ν_{17} and ν_{30}) would also exhibit vibronic coupling only now it will be pJT rather than JT effect. This is the reason the experimentally observed FCFs of both the ν_{30} and ν_{17} bands in the LIF spectra are

drastically higher than the calculated values. These ideas parallel our previous discussion of the spin-vibronic effects in the spectrum of CaOCH_3 and CaOC_2H_5 .^{10, 42}

3.4. Cavity Ring-Down (CRD) Spectrum and Vibrational Branching Ratios (VBRs)

A separate CRD spectroscopy measurement was performed to measure the extent of power saturation of the origin transition in the LIF spectrum and better determine the FCFs and VBRs experimentally. The LIF and CRD spectra of the origin and the 15_0^1 bands are compared in Figure 5.

The relative intensities of vibronic bands in the LIF/DF and CRD spectra have been used to determine the FCFs and VBRs using the method described in our previous work on the calcium methoxide and calcium ethoxide radicals.^{10, 42} The FCFs of the $\tilde{A}_1^2A'/\tilde{A}_2^2A'' \leftarrow \tilde{X}^2A'$ transition and the FCFs and VBRs of the $\tilde{A}_1^2A' \rightarrow \tilde{X}^2A'$ transition are summarized in Table 4. The VBR of the origin band is 0.746, compared to 0.904 for the $\tilde{A}^2E_{1/2} \rightarrow \tilde{X}^2A'$ transition of calcium methoxide,¹⁰ and 0.858 for the $\tilde{A}_1^2A'' \rightarrow \tilde{X}^2A'$ transition of calcium ethoxide.⁴² (See Table 3.) Therefore, a more complex photon recycling scheme would be needed to do direct laser-cool calcium isopropoxide molecules.

4. Discussion and Conclusions

To summarize, we report vibrationally resolved LIF/DF and CRD spectra of the $\tilde{A}_1^2A'/\tilde{A}_2^2A'' - \tilde{X}^2A'$ transition of the calcium isopropoxide radical under jet-cooled conditions. The \tilde{A}_2

– \tilde{A}_1 separation of calcium isopropoxy is almost the same as calcium ethoxide, but the symmetries of the higher- and lower-energy states are interchanged. The vibrational assignment has been made on the basis of CASSCF- and EOM-CCSD-calculated vibrational frequencies and FCFs. In general, the EOM-CCSD calculations provide a more accurate prediction of both vibrational frequencies and intensities of the electronically allowed transitions and show clearly the importance of subtle changes in the chemical bonding between the two electronic states for the spectroscopy. For example, the in-plane bending mode (ν_{17}) is coupled to a vibrational mode with the in-plane CaOC bending character (ν_{10}) due to a slight change of the CaOC bond angle upon the electronic excitation and the Duschinsky mixing. However, some effects like the transition to the $\nu^{\nu}=1$ level of the out-of-plane CaOC bending mode (ν_{30}) with a'' symmetry, which was observed in the LIF spectrum, must be attributed to vibronic interactions like the pJT interaction, which are not included in the electronic calculations.

It is important to note that about five years ago, Kozyryev *et al.*^{3, 16} made a pioneering proposal for laser cooling of complex polyatomic molecules, including $\text{CaOCH}(\text{CH}_3)_2$. They developed a simplified model to predict the FCFs for the origin band of a number of molecules of the form MOR where the metal M = Ca or Sr and OR is an alkoxy group. This model considers that only a single Ca-O stretch mode steals intensity from the origin and found an origin FCF value of >95% for $\text{CaOCH}(\text{CH}_3)_2$ compared to the experimental value of 75% in Table 4. The present experimental work on $\text{CaOCH}(\text{CH}_3)_2$ and our earlier work^{10, 42} on CaOCH_3 and CaOC_2H_5 have shown that modes other than the Ca-O stretch steal intensity from the origin. One set, e.g., ν_9 - ν_{11} , ν_{14} , and ν_{15} , demonstrates that modes other than the Ca-O stretch (ν_{13}), particularly ones with the CaOC bending character, participate to some degree in the chemical bonding and have their vibrational potentials altered by the $\tilde{A} \leftarrow \tilde{X}$ electronic transition, which

results in significant non-diagonal FCFs for transitions to vibrational levels of these modes. Another set of modes, e.g., ν_{17} and ν_{30} , depends on spin-vibronic couplings to provide their intensity. These effects do not necessarily preclude the previously predicted possibilities for laser cooling of polyatomic molecules, but they do make the experiments more challenging.

In any future laser-cooling experiment, pre-cooled calcium isopropoxide molecules are excited from the \tilde{X}^2A' state to the \tilde{A}_1^2A' state. Following the excitation of the origin transition, spontaneous emission to excited vibrational levels of the ground electronic state occurs due to off-diagonal transitions (see Figure 3a), causing loss of population from the cooling cycle. One may use four repumping lasers to return the population from the ground-state $\nu''=1$ levels of the ν_{15} , ν_{14} , ν_{13} , and ν_{10} modes to the cooling cycle. The combined VBRs of the spontaneous decay to the vibrational ground level and the aforementioned four vibrational levels of the \tilde{X}^2A' state is 0.950. As a result, a molecule will experience, on average, ~ 20 scattering events before it decays to vibrational “dark” states that are not addressed by the repumping lasers.

One of the most important molecular properties related to direct laser cooling of alkaline earth monoalkoxide radicals is the VBR of the $\tilde{A}^2E_{1/2} \rightarrow \tilde{X}^2A_1$ (for C_{3v} molecules) or $\tilde{A}_1 \rightarrow \tilde{X}$ (for molecules with lower symmetries) origin transition. In Table 3, experimentally determined and calculated origin-band VBRs of calcium methoxide, ethoxide, and isopropoxide radicals are compared. The experimental VBR drops from 0.904 for CaOCH_3 to 0.858 for CaOC_2H_5 , then to 0.746 for $\text{CaOCH}(\text{CH}_3)_2$ due to the lowered symmetry of the molecule and the increasing number of vibrational modes. For CaOCH_3 (C_{3v}), both CASSCF and EOM-CCSD calculations predict the VBR with considerable accuracy (within 5%). Indeed, the CASSCF calculation predicts the VBR to within 1%, thanks to the high symmetry of the molecule and an active space

that includes all molecular orbitals with significance to the $\tilde{A}^2E - \tilde{X}^2A_1$ electronic transition. Inclusion of SO and vibronic (JT and pJT) interactions does not significantly affect the VBR of the origin transition (from 0.936 to 0.933), although it does accurately predict intensities for transitions to levels of JT and pJT-active modes that would otherwise be forbidden.¹⁰ For CaOC_2H_5 (C_s), the CASSCF calculation provides a less accurate prediction of the VBR of the origin transition than EOM-CCSD due to the lowered symmetry and the limited active space. The inclusion of SO and pJT interactions improves the accuracy of the prediction (from within 5% to $\sim 3.5\%$). For $\text{CaOCH}(\text{CH}_3)_2$ (C_s), both CASSCF and EOM-CCSD calculations significantly overestimate the VBR of the origin transition (by $\sim 17\%$) for reasons described in the preceding paragraph. We expect that future multi-state, multimode spin-vibronic calculations will provide more reliable predictions of VBRs for asymmetric-top molecules. Nevertheless, our experimental and computational work on the calcium methoxide, ethoxide, and isopropoxide radicals suggests that molecules with higher symmetry, fewer vibrational modes involved in the chemical bonding, and weaker vibronic interactions between degenerate or nearly degenerate states are more amenable to direct laser-cooling.

It is worth noting that the relative intensity of a transition can only be considered to be proportional to its FCF if the variation of the electronic transition moment with geometric change is negligible *and* the BO approximation is valid. In Section 3, we discuss the possibility that some transitions primarily (e.g., ν_{17}) or exclusively (e.g., ν_{30}) gain their intensity *via* spin-vibronic interactions that violate the BO approximation. For this reason, in Table 4, experimental FCFs are summed over both $\tilde{A}_1^2A' \rightarrow \tilde{X}^2A'$ and $\tilde{A}_2^2A'' \rightarrow \tilde{X}^2A'$ transitions before being normalized to unity, which minimizes the effect of spin-vibronic interactions between the \tilde{A}_1 and \tilde{A}_2 states. However, if the vibronic interactions allow intensity borrowing from states out of the \tilde{A}_1/\tilde{A}_2

system, like the nearby \tilde{B} state, then the experimental FCFs would not need to sum to unity, but greater than it. In our previous work on CaOCH_3 and CaOC_2H_5 , spin-vibronic calculations predicted that the pJT interactions between the \tilde{A} and \tilde{B} states do make contributions to the observed transitions to the $\nu=1$ levels of the pJT-active CaOC bending modes. In the present work on $\text{CaOCH}(\text{CH}_3)_2$, similar spin-vibronic calculations haven't been accomplished. However, transitions to the CaOC bending levels (ν_{17} and ν_{30}) may have gained considerable intensity from the $\tilde{B} - \tilde{A}$ interaction. Neglect of the $\tilde{B} - \tilde{A}$ interaction leads to an underestimation of FCFs for transitions to vibrational levels of non-pJT modes. Given that 17_0^1 and 30_0^1 both have FCFs ~ 0.05 , the origin-band FCF may be underestimated by up to $\sim 10\%$.

More experimental and computational investigations on calcium isopropoxide would be useful to understand better its spectroscopy and electronic/vibronic structure, as well as to understand how trends in such structure may influence whether a molecule is a good candidate for direct laser-cooling. First, higher sensitivity of the spectroscopic measurement is desired. In the present LIF and DF measurements, transitions with FCFs less than ~ 0.002 are not observed, which limits the accuracy of experimentally determined FCFs and VBRs. According to the EOM-CCSD calculations, FCFs of the observed transitions in the DF spectra sum to ~ 0.984 , implying that experimental FCFs tabulated in Table 4 are all overestimated by $\sim 1.6\%$ due to this reason. Other experimental methods like that implemented in Ref. [91] may be used to detect weak transitions and determine their FCFs and VBRs.

LIF and CRD spectroscopy measurements with continuous-wave (CW) lasers or laser amplifiers seeded by CW lasers can be used to resolve the \tilde{A} -state rotational and fine structure, while that of the \tilde{X} -state can be resolved in the SEP spectroscopy measurement using narrow-linewidth laser systems.^{87, 92-94} Spectroscopic measurements with CW lasers will also improve

the sensitivity and accuracy of experimentally determined FCFs and VBRs. Rotationally resolved spectra of jet-cooled calcium isopropoxide radicals, as well as calcium ethoxide, are strongly desired for multiple reasons. First, the contributions to the observed $\tilde{A}_2 - \tilde{A}_1$ splitting from SO coupling and the ZPE-corrected difference potential (Eq. 1) can be determined independently by fitting the rotational and fine structure.^{43, 44} Second, the details of the pJT effect can be revealed *via* rotational analysis.⁷⁶ Moreover, rotational constants determined in fitting the rotational structure can be used to benchmark *ab initio* calculations. Finally, experimentally determined rotational and fine structure is a prerequisite to designing the rotational closure for future laser-cooling experiments.

Conflicts of interest

The authors declare that they have no known competing financial interests or personal relationships that could have appeared to influence the work reported in this paper.

Acknowledgments

The authors would like to thank the two anonymous reviewers for their comments and suggestions that helped improve this paper significantly. This work was supported by the National Science Foundation under grant numbers CHE-1454825 and CHE-1955310. K.S. gratefully acknowledges a Terry A. Miller Postdoctoral Fellowship from the Ohio State

University. T.A.M. acknowledges support from the Ohio Supercomputer *via* Project No. PAS0540.

Table 1: Geometric parameters, rotational constants, and $\tilde{A}_1^2A'/\tilde{A}_2^2A'' \leftarrow \tilde{X}^2A'$ excitation energies of the $\text{CaOCH}(\text{CH}_3)_2$ radicals calculated at the CASSCF(3,6)/cc-pVTZ and EOMEA-CCSD/cc-pVTZ levels of theory.

	CASSCF ^a		EOM-CCSD ^b		
	\tilde{X}	\tilde{A}_1/\tilde{A}_2	\tilde{X}	\tilde{A}_1	\tilde{A}_2
r_{CaO} (Å)	2.016	1.991	2.006	1.975	1.975
r_{CO} (Å)	1.375	1.381	1.384	1.388	1.388
r_{CC} (Å)	1.527	1.525	1.520	1.518	1.518
$\angle\text{CaOC}$ (deg.)	180.0	179.5	178.4	178.0	178.5
$\angle\text{OCC}$ (deg.)	110.8	110.9	110.3	110.1	110.1
Φ_{CCOC}	123.8	124.9	118.6	118.6	118.5
A (GHz)	7.988	7.970	8.012	8.003	8.003
B (GHz)	1.586	1.602	1.597	1.622	1.622
C (GHz)	1.390	1.401	1.403	1.424	1.424
T_e (cm ⁻¹)		15452 ^{c,d}		16043 ^e	16077 ^f

a. Calculated at the SA-CASSCF(3,6)/cc-pVTZ level of theory.

b. Calculated at the EOMEA-CCSD/cc-pVTZ level of theory.

c. Defined as the energy separation between the \tilde{X}^2A' state and the center of the \tilde{A}_1^2A' and \tilde{A}_2^2A'' states.

d. Compared to the experimental value of 15844 cm⁻¹.

e. Compared to the experimental value of 15810 cm⁻¹.

f. Compared to the experimental value of 15878 cm⁻¹.

Table 2. Harmonic vibrational frequencies of the \tilde{X}^2A' and $\tilde{A}_1^2A'/\tilde{A}_2^2A''$ states of the $\text{CaOCH}(\text{CH}_3)_2$ radical calculated at the (SA-)CASSCF(3,6)/cc-pVTZ and EOMEA-CCSD/cc-pVTZ levels of theory compared to experimentally determined values. Vibrational modes are numbered following the Herzberg convention.

Mode	sym.	CASSCF ^a		EOM-CCSD ^b			Expt.		Description
		\tilde{X}	\tilde{A}	\tilde{X}	\tilde{A}_1 st	\tilde{A}_2	\tilde{X}	\tilde{A}	
ν_1	a'	3207	3243	3126	3129	3129			
ν_2	a'	3204	3195	3121	3124	3125			
ν_3	a'	3146	3141	3065	3067	3068			
ν_4	a'	3063	3056	2990	3007	3006			
ν_5	a'	1621	1623	1535	1536	1535			
ν_6	a'	1607	1604	1523	1524	1523			
ν_7	a'	1540	1544	1428	1431	1432			
ν_8	a'	1520	1522	1408	1407	1408			
ν_9	a'	1327	1321	1257	1252	1251	1181		CaOC asym. stretch+umbrella
ν_{10}	a'	1278	1278	1203	1205	1204	1100		with in-plane CaOC bending character
ν_{11}	a'	1127	1125	1063	1066	1066	1015		CaOC asym. stretch+umbrella
ν_{12}	a'	893	894	870	875	875		842	symmetric CC stretch
ν_{13}	a'	586	592	551	560	561	543	556	CaO stretch+CaOC bending
ν_{14}	a'	461	462	442	447	447	432	443	CCC bending+CaOC bending
ν_{15}	a'	333	334	322	326	326	312	318	CCC bending+CaOC bending
ν_{16}	a'	298	286	295	296	294			in-phase double methyl rotation
ν_{17}	a'	120	126	105	104	110	96	101	in-plane CaOC bending
ν_{18}	a''	3203	3241	3119	3121	3123			
ν_{19}	a''	3191	3198	3115	3118	3120			
ν_{20}	a''	3138	3148	3060	3062	3063			
ν_{21}	a''	1601	1608	1515	1512	1526			
ν_{22}	a''	1596	1592	1512	1505	1513			
ν_{23}	a''	1521	1527	1421	1420	1428			
ν_{24}	a''	1484	1491	1396	1394	1399			
ν_{25}	a''	1227	1229	1179	1181	1181			
ν_{26}	a''	1002	1007	952	955	955			
ν_{27}	a''	985	987	931	934	934			
ν_{28}	a''	480	480	456	457	455			
ν_{29}	a''	255	239	256	255	254			out-of-phase double methyl rotation
ν_{30}	a''	95	102	85	87	87	81	83	out-of-plane CaOC bending

- Calculated at the SA-CASSCF(3,6)/cc-pVTZ level of theory.
- Calculated at the EOMEA-CCSD/cc-pVTZ level of theory.

Table 3. Experimental and calculated values of the SO-free $\tilde{A}_2 - \tilde{A}_1$ separation (ΔE_0), the vibronically quenched SO separation of the \tilde{A} state ($a\zeta_e d$), the overall $\tilde{A}_2 - \tilde{A}_1$ separation ($\Delta E^{\tilde{A}_2 - \tilde{A}_1} = \sqrt{(a\zeta_e d)^2 + (\Delta E_0)^2}$), the $\tilde{A} - \tilde{X}$ excitation energy $\Delta E^{\tilde{A} - \tilde{X}}$, and the VBR of the origin transition for calcium methoxide, ethoxide, and isopropoxide radicals.

		CaOCH ₃	CaOC ₂ H ₅	CaOCH(CH ₃) ₂
		Ref. [10]	Ref. [42]	present work
ΔE_0 (cm ⁻¹)	Expt.	0		
	EOM-CCSD	0	17	-34
$a\zeta_e d$ (cm ⁻¹)	Expt.	67		
	EOM-CCSD	66	60	58 ^d
$\Delta E^{\tilde{A}_2 - \tilde{A}_1}$ (cm ⁻¹)	Expt	67	67	68
	EOM-CCSD	66	62	
$\Delta E^{\tilde{A} - \tilde{X}}$ (cm ⁻¹)	Expt. ^a	15925	15882	15844
	CASSCF ^{b,c}	15359 [1.037]	15390 [1.032]	15452 [1.025]
	EOM-CCSD ^{b,c}	15918 [1.0004]	15869 [1.0008]	16060 [0.9866]
VBR of Origin	Expt.	0.904	0.858	0.746
	CASSCF ^c	0.902 [1.0022]	0.928 [0.9246]	0.878 [0.8497]
	EOM-CCSD ^c	0.936 [0.9658]	0.901 [0.9523]	0.871 [0.8565]
	Spin-vibronic ^c	0.933 [0.9689]	0.888 [0.9662]	

a. T_{00} for experimental values.

b. T_e for calculated values.

c. In squared parentheses are scaling factors for the calculated value to match the experimental value.

d. Calculated using experimental $\Delta E^{\tilde{A}_2 - \tilde{A}_1}$ and EOM-CCSD-calculated ΔE_0 . (See Eq. 1.)

Table 4. FCFs and VBRs determined in the experimental LIF/DF and CRD spectra of calcium isopropoxide compared to the calculated values. See text for discussion.

$\tilde{A}_1^2A'/\tilde{A}_2^2A'' \leftarrow \tilde{X}^2A'$				$\tilde{A}_1^2A' \rightarrow \tilde{X}^2A'$						
Transition	FCF=VBR			Transition	FCF			VBR		
	Cal'd ^a	Cal'd ^b	Expt. (LIF/CRD)		Cal'd ^a	Cal'd ^b	Expt. (DF)	Cal'd ^a	Cal'd ^b	Expt. (DF)
0_0^0	0.864	0.861	0.721 ^c	0_0^0	0.866	0.861	0.721 ^d	0.878	0.871	0.746
30_0^1			0.051							
17_0^1		0.008	0.051	17_1^0		0.007	0.012		0.007	0.013
30_0^2			0.044							
16_0^1	0.043	0.003		16_1^0	0.038	0.004		0.036	0.004	
15_0^1	0.019	0.043	0.070	15_1^0	0.027	0.049	0.062	0.026	0.047	0.060
14_0^1	0.006	0.030	0.028	14_1^0	0.005	0.033	0.056	0.005	0.031	0.053
13_0^1	0.030	0.027	0.027	13_1^0	0.028	0.023	0.039	0.025	0.021	0.036
$13_0^1 16_0^1$	0.002									
12_0^1	0.003	0.003	0.008	12_1^0	0.003	0.003		0.003	0.003	
$13_0^1 15_0^1$	0.001									
				11_1^0	0.002	0.004	0.020	0.002	0.003	0.017
				10_1^0	0.006		0.066	0.005		0.055
				9_1^0	0.009	0.007	0.025	0.007	0.006	0.020
				6_1^0	0.003			0.002		
				5_1^0	0.004			0.004		

- Calculated at the CASSCF(3,6)/cc-pVTZ level of theory.
- Calculated at the EOMEA-CCSD/cc-pVTZ level of theory. $\tilde{A}_1^2A' - \tilde{X}^2A'$ transition only.
- Determined using both LIF and CRD spectra. See Refs. [10] and [42] for details.
- Fixed to that of the $\tilde{A}_1^2A'/\tilde{A}_2^2A'' \leftarrow \tilde{X}^2A'$ origin transition determined using the LIF and CRD spectra. See Refs. [10] and [42] for details.

Figure 1. The molecular orbitals of $\text{CaOCH}(\text{CH}_3)_2$ included in the CASSCF calculations.

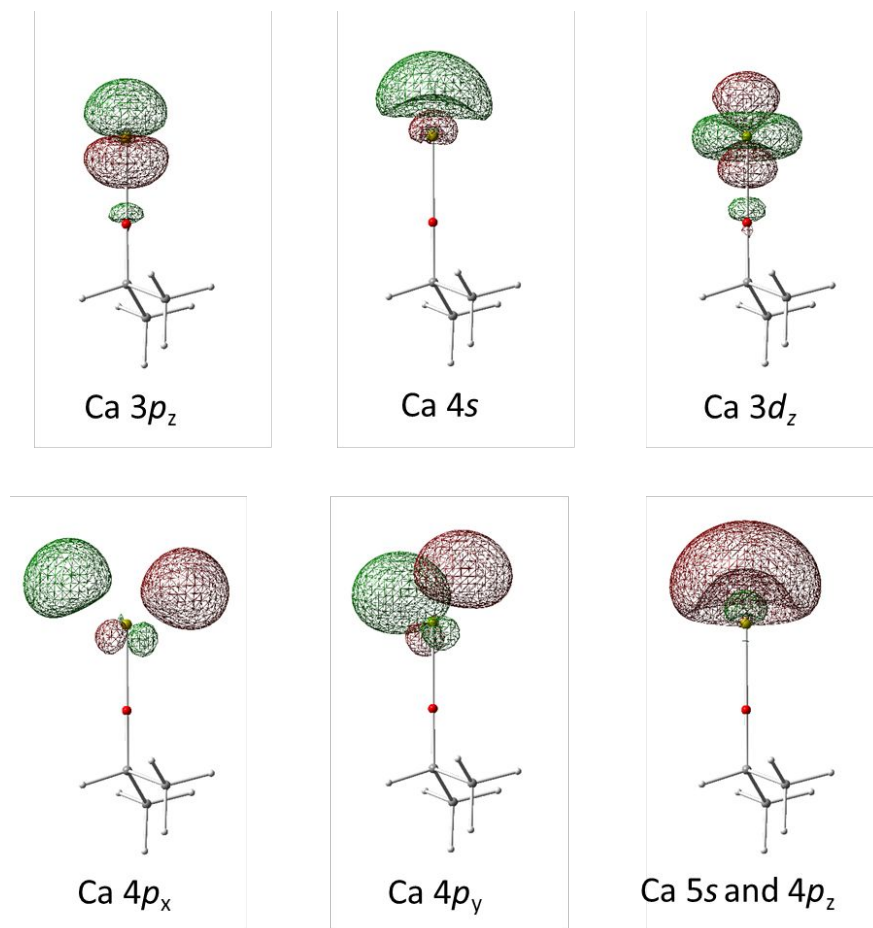


Figure 2. (a) The experimentally obtained $\tilde{A}_1^2A'/\tilde{A}_2^2A''\leftarrow\tilde{X}^2A'$ LIF spectrum of $\text{CaOCH}(\text{CH}_3)_2$. Wavenumbers are relative to the center of the origin band at 15844 cm^{-1} . Simulations using the transition frequencies and intensities calculated at the (b) EOMEA-CCSD/cc-pVTZ and (c) SA-CASSCF(3,6)/cc-pVTZ levels of theory. The EOM-CCSD-calculated $\tilde{A}_1^2A'\leftarrow\tilde{X}^2A'$ and $\tilde{A}_2^2A''\leftarrow\tilde{X}^2A'$ spectra are shifted by -34 and 34 cm^{-1} , respectively, to match the origin bands in the experimental spectrum. The CASSCF-calculated spectrum is SO-free.

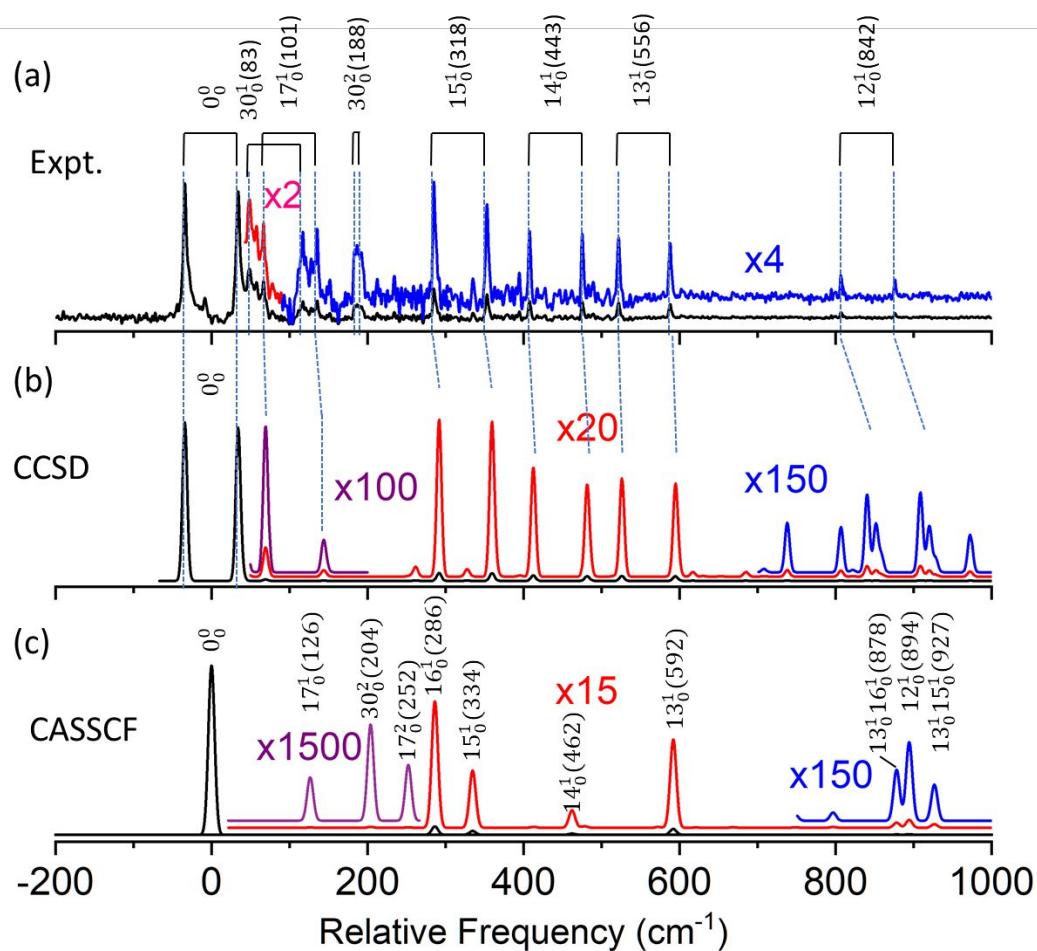


Figure 3. Experimental DF spectra of $\text{CaOCH}(\text{CH}_3)_2$ obtained by pumping the (a) $\tilde{A}_1^2A' \leftarrow \tilde{X}^2A'$ and (c) $\tilde{A}_2^2A'' \leftarrow \tilde{X}^2A'$ origin transitions in its LIF spectrum. Wavenumbers are red-shifts relative to the pumped origin transitions. The asterisked peaks are due to collision-induced population transfer between the \tilde{A}_1^2A' and \tilde{A}_2^2A'' states. Simulated DF spectra of (b) $\tilde{A}_1^2A' \rightarrow \tilde{X}^2A'$ and (d) $\tilde{A}_2^2A'' \rightarrow \tilde{X}^2A'$ transitions with transition frequencies and intensities calculated at the EOMEA-CCSD/cc-pVTZ level of theory. (e) The $\tilde{A}_1^2A'/\tilde{A}_2^2A'' \rightarrow \tilde{X}^2A'$ DF spectrum simulated with transition frequencies and intensities calculated at the (SA-)CASSCF(3,6)/cc-pVTZ level of theory.

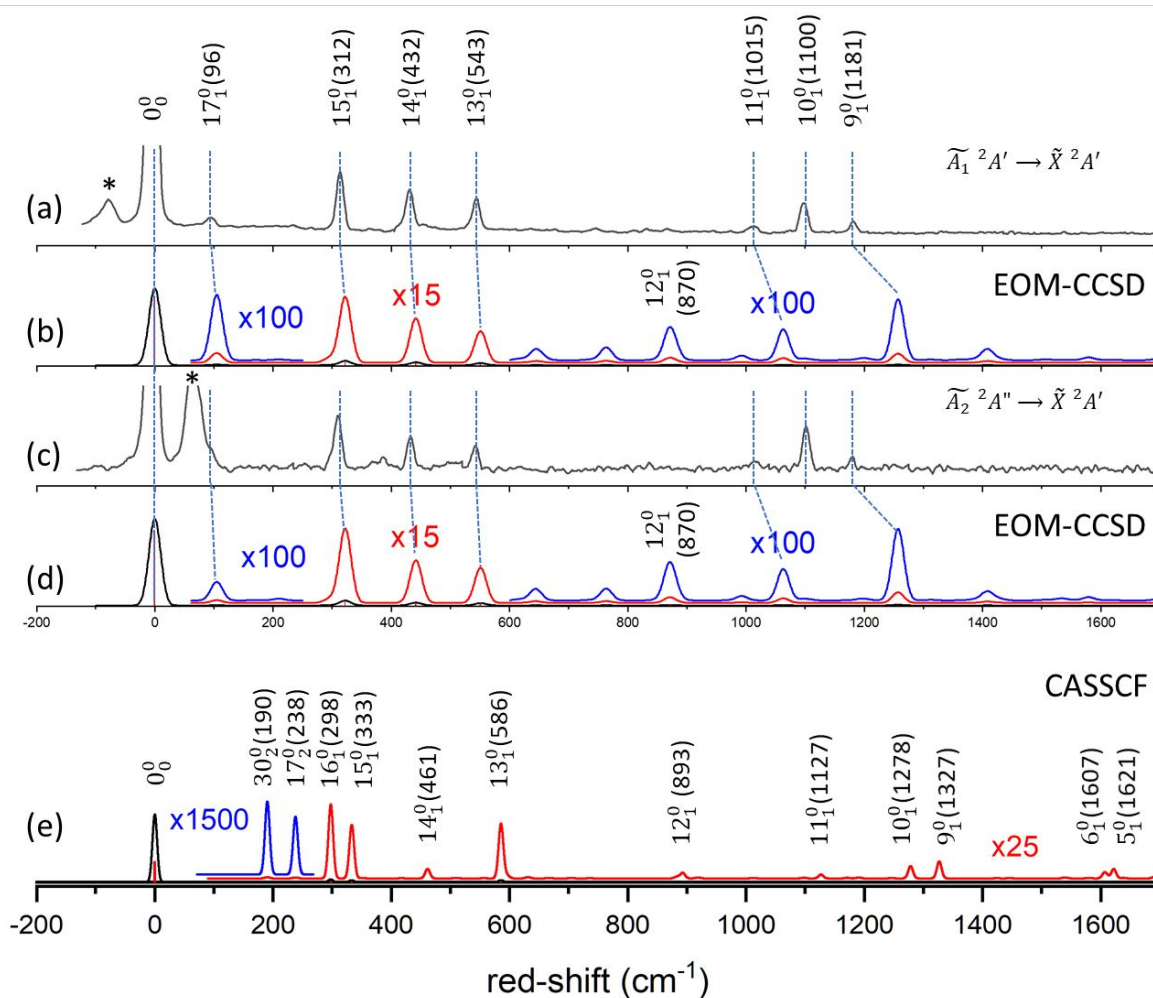


Figure 4. DF spectra of $\text{CaOCH}(\text{CH}_3)_2$ obtained by pumping different vibronic bands in its $\tilde{A}_1^2 A' / \tilde{A}_2^2 A'' \leftarrow \tilde{X}^2 A'$ LIF spectrum. The peaks at 608, 687, and 1235 cm^{-1} red shifts were observed only when the vibronic band at 188 cm^{-1} in the LIF spectrum was pumped, and their assignments (in bold font) are tentative. (See text.)

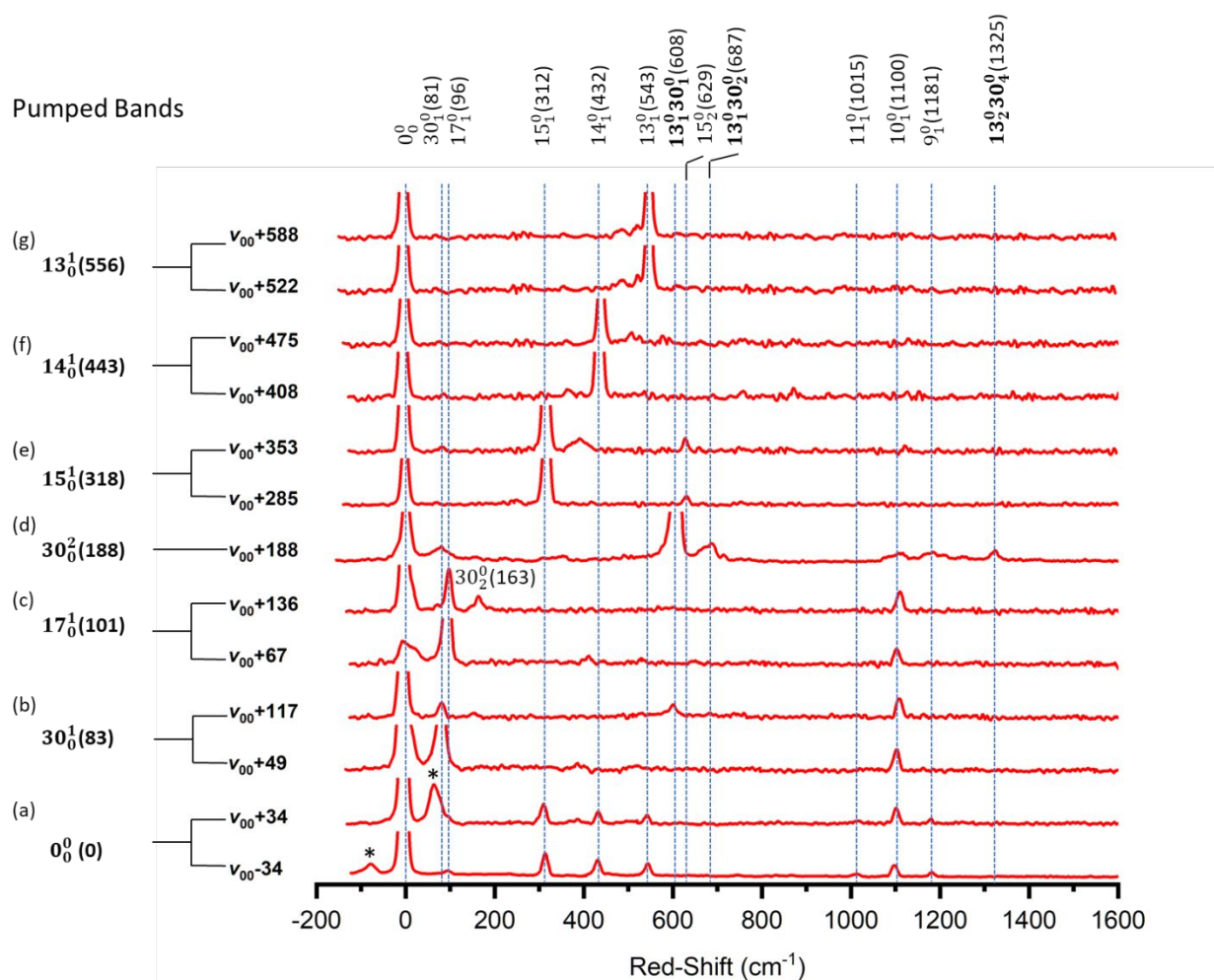
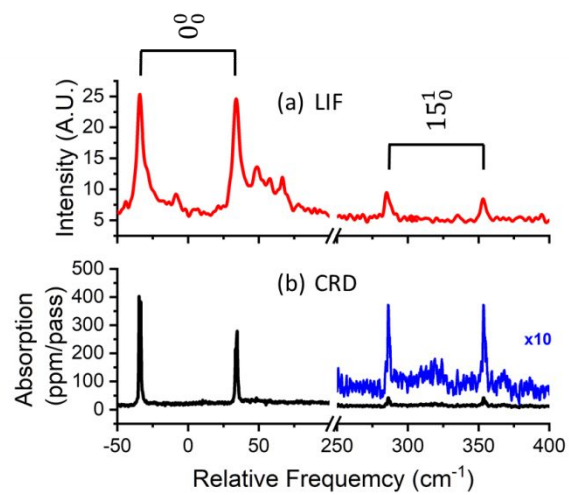


Figure 5. Comparison of (a) LIF and (b) CRD spectra of $\text{CaOCH}(\text{CH}_3)_2$ that shows the power saturation of the origin transitions in the LIF measurement.



References:

1. M. D. Di Rosa, *Eur. Phys. J. D*, 2004, **31**, 395-402.
2. T. A. Isaev and R. Berger, *Phys. Rev. Lett.*, 2016, **116**, 063006.
3. I. Kozyryev, L. Baum, K. Matsuda and J. M. Doyle, *ChemPhysChem*, 2016, **17**, 3641-3648.
4. D. Mitra, N. B. Vilas, C. Hallas, L. Anderegg, B. L. Augenbraun, L. Baum, C. Miller, S. Raval and J. M. Doyle, *Science*, 2020, **369**, 1366.
5. C. R. Brazier, L. C. Ellingboe, S. Kinsey-Nielsen and P. F. Bernath, *J. Am. Chem. Soc.*, 1986, **108**, 2126-2132.
6. P. F. Bernath, *Science*, 1991, **254**, 665.
7. I. B. Bersuker, *The Jahn-Teller Effect*, Cambridge University Press, 2006.
8. T. A. Barckholtz and T. A. Miller, *Int. Rev. Phys. Chem.*, 1998, **17**, 435-524.
9. I. Kozyryev, T. C. Steimle, P. Yu, D.-T. Nguyen and J. M. Doyle, *New J. Phys.*, 2019, **21**, 052002.
10. A. C. Paul, K. Sharma, M. A. Reza, H. Telfah, T. A. Miller and J. Liu, *J. Chem. Phys.*, 2019, **151**, 134303.
11. M. Elhanine, R. Lawruszczuk and B. Soep, *Chem. Phys. Lett.*, 1998, **288**, 785-792.
12. K.-i. C. Namiki, J. S. Robinson and T. C. Steimle, *J. Chem. Phys.*, 1998, **109**, 5283-5289.
13. P. Crozet, F. Martin, A. J. Ross, C. Linton, M. J. Dick and A. G. Adam, *J. Mol. Spectrosc.*, 2002, **213**, 28-34.
14. P. Crozet, A. J. Ross, C. Linton, A. G. Adam, W. S. Hopkins and R. J. L. Roy, *J. Mol. Spectrosc.*, 2005, **229**, 224-230.
15. C. J. Whitham, S. A. Beaton, Y. Ito and J. M. Brown, *J. Mol. Spectrosc.*, 1998, **191**, 286-294.
16. B. L. Augenbraun, J. M. Doyle, T. Zelevinsky and I. Kozyryev, *Phys. Rev. X*, 2020, **10**, 031022.
17. M. Li, J. Kłos, A. Petrov and S. Kotochigova, *Commun. Phys.*, 2019, **2**, 148.
18. J. Kłos and S. Kotochigova, *Phys. Rev. Research*, 2020, **2**, 013384.
19. M. V. Ivanov, F. H. Bangerter, P. Wójcik and A. I. Krylov, *J. Phys. Chem. Lett.*, 2020, **11**, 6670-6676.
20. C. E. Dickerson, H. Guo, G.-Z. Zhu, E. R. Hudson, J. R. Caram, W. C. Campbell and A. N. Alexandrova, *J. Phys. Chem. Lett.*, 2021, **12**, 3989-3995.
21. C. E. Dickerson, H. Guo, A. J. Shin, B. L. Augenbraun, J. R. Caram, W. C. Campbell and A. N. Alexandrova, *Phys. Rev. Lett.*, 2021, **126**, 123002.
22. K. K. Ni, S. Ospelkaus, M. H. G. de Miranda, A. Pe'er, B. Neyenhuis, J. J. Zirbel, S. Kotochigova, P. S. Julienne, D. S. Jin and J. Ye, *Science*, 2008, **322**, 231-235.
23. M. T. Bell and T. P. Softley, *Mol. Phys.*, 2009, **107**, 99-132.
24. M. Hutson Jeremy, *Science*, 2010, **327**, 788-789.
25. S. Ospelkaus, K. K. Ni, D. Wang, M. H. G. de Miranda, B. Neyenhuis, G. Quéméner, P. S. Julienne, J. L. Bohn, D. S. Jin and J. Ye, *Science*, 2010, **327**, 853-857.
26. L. R. Liu, J. D. Hood, Y. Yu, J. T. Zhang, N. R. Hutzler, T. Rosenband and K. K. Ni, *Science*, 2018, **360**, 900-903.
27. D. DeMille, *Phys. Rev. Lett.*, 2002, **88**, 067901.
28. D. Patterson, *Phys. Rev. A*, 2018, **97**, 033403.
29. J. J. Hudson, B. E. Sauer, M. R. Tarbutt and E. A. Hinds, *Phys. Rev. Lett.*, 2002, **89**, 023003.
30. E. R. Meyer, J. L. Bohn and M. P. Deskevich, *Phys. Rev. A*, 2006, **73**, 062108.
31. H. Loh, K. C. Cossel, M. C. Grau, K. K. Ni, E. R. Meyer, J. L. Bohn, J. Ye and E. A. Cornell, *Science*, 2013, **342**, 1220-1222.
32. J. Baron, W. C. Campbell, D. DeMille, J. M. Doyle, G. Gabrielse, Y. V. Gurevich, P. W. Hess, N. R. Hutzler, E. Kirilov, I. Kozyryev, B. R. O'Leary, C. D. Panda, M. F. Parsons, E. S. Petrik, B. Spaun, A. C. Vutha and A. D. West, *Science*, 2014, **343**, 269-272.

33. W. B. Cairncross, D. N. Gresh, M. Grau, K. C. Cossel, T. S. Roussy, Y. Ni, Y. Zhou, J. Ye and E. A. Cornell, *Phys. Rev. Lett.*, 2017, **119**, 153001.
34. D. DeMille, M. Doyle John and O. Sushkov Alexander, *Science*, 2017, **357**, 990-994.
35. I. Kozyryev and N. R. Hutzler, *Phys. Rev. Lett.*, 2017, **119**, 133002.
36. V. Andreev, D. G. Ang, D. DeMille, J. M. Doyle, G. Gabrielse, J. Haefner, N. R. Hutzler, Z. Lasner, C. Meisenhelder, B. R. O'Leary, C. D. Panda, A. D. West, E. P. West, X. Wu and A. Collaboration, *Nature*, 2018, **562**, 355-360.
37. L. Anderegg, W. Cheuk Lawrence, Y. Bao, S. Burchesky, W. Ketterle, K.-K. Ni and M. Doyle John, *Science*, 2019, **365**, 1156-1158.
38. W. B. Cairncross and J. Ye, *Nature Reviews Physics*, 2019, **1**, 510-521.
39. L. D. Carr, D. DeMille, R. V. Krems and J. Ye, *New J. Phys.*, 2009, **11**, 055049.
40. G. Quéméner and P. S. Julienne, *Chem. Rev.*, 2012, **112**, 4949-5011.
41. H. Köppel, W. Domcke and L. S. Cederbaum, in *Conical Intersections*, WORLD SCIENTIFIC, 2004, vol. Volume 15, pp. 323-367.
42. A. C. Paul, K. Sharma, H. Telfah, T. A. Miller and J. Liu, *J. Chem. Phys.*, 2021, **155**, 024301.
43. J. Liu, *J. Chem. Phys.*, 2018, **148**, 124112.
44. Y. Yan, K. Sharma, T. A. Miller and J. Liu, *J. Chem. Phys.*, 2020, **153**, 174306.
45. R. Chhantyal-Pun, M. Roudjane, D. G. Melnik, T. A. Miller and J. Liu, *J. Phys. Chem. A*, 2014, **118**, 11852-11870.
46. J. Liu, D. Melnik and T. A. Miller, *J. Chem. Phys.*, 2013, **139**, 094308.
47. X. Q. Tan, J. M. Williamson, S. C. Foster and T. A. Miller, *J. Phys. Chem.*, 1993, **97**, 9311-9316.
48. P. D. A. Mills, C. M. Western and B. J. Howard, *J. Phys. Chem.*, 1986, **90**, 3331-3338.
49. W. M. Fawzy and J. T. Hougen, *J. Mol. Spectrosc.*, 1989, **137**, 154-165.
50. M. D. Marshall and M. I. Lester, *J. Chem. Phys.*, 2004, **121**, 3019-3029.
51. C. S. Brauer, G. Sedo, E. M. Grumstrup, K. R. Leopold, M. D. Marshall and H. O. Leung, *Chem. Phys. Lett.*, 2005, **401**, 420-425.
52. M. D. Marshall and M. I. Lester, *J. Phys. Chem. B*, 2005, **109**, 8400-8406.
53. G. E. Doublerly, P. L. Raston, T. Liang and M. D. Marshall, *J. Chem. Phys.*, 2015, **142**, 134306.
54. F. J. Hernandez, J. T. Brice, C. M. Leavitt, G. A. Pino and G. E. Doublerly, *J. Phys. Chem. A*, 2015, **119**, 8125-8132.
55. L. Yu, D. W. Cullin, J. M. Williamson and T. A. Miller, *J. Chem. Phys.*, 1993, **98**, 2682-2698.
56. H. J. Wörner and F. Merkt, *J. Chem. Phys.*, 2007, **126**, 154304.
57. M. Grütter, H. J. Wörner and F. Merkt, *J. Chem. Phys.*, 2009, **131**, 024309.
58. J. Liu and T. A. Miller, *J. Phys. Chem. A*, 2014, **118**, 11871-11890.
59. L. Zu, J. Liu, G. Tarczay, P. Dupré and T. A. Miller, *J. Chem. Phys.*, 2004, **120**, 10579-10593.
60. J. Liu, M.-W. Chen and T. A. Miller, *J. Phys. Chem. A*, 2021, **125**, 1402-1412.
61. J. Liu and T. A. Miller, *J. Phys. Chem. A*, 2021, **125**, 1391-1401.
62. J. F. Stanton, J. Gauss, L. Cheng, M. E. Harding, D. A. Matthews and P. G. Szalay, *CFOUR, Coupled-Cluster techniques for Computational Chemistry, a quantum-chemical program package*. <http://www.cfour.de/>.
63. V. A. Mozhayskiy and A. I. Krylov, *ezSpectrum* <http://iopshell.usc.edu/downloads>.
64. S. Gozem and A. I. Krylov, *WIREs Computational Molecular Science*, 2021, DOI: <https://doi.org/10.1002/wcms.1546>, e1546.
65. S. M. Rabidoux, V. Eijkhout and J. F. Stanton, *J. Chem. Theory Comput.*, 2016, **12**, 728-739.
66. F. Duschinsky, *Acta Physicochimica URSS*, **7**, 551-566.
67. H. Köppel, W. Domcke and L. S. Cederbaum, in *Adv. Chem. Phys.*, eds. I. Prigogine and S. A. Rice, John Wiley & Sons, New York, 1984, vol. 57, pp. 59-246.
68. H. Guo, G. Worth and W. Domcke, *J. Chem. Phys.*, 2021, **155**, 080401.

69. Y. Guan, C. Xie, D. R. Yarkony and H. Guo, *Phys. Chem. Chem. Phys.*, 2021, **23**, 24962-24983.
70. S. Matsika, *Chem. Rev.*, 2021, **121**, 9407-9449.
71. J. F. Stanton, *J. Chem. Phys.*, 2007, **126**, 134309.
72. J. F. Stanton, *Mol. Phys.*, 2009, **107**, 1059-1075.
73. J. F. Stanton and M. Okumura, *Phys. Chem. Chem. Phys.*, 2009, **11**, 4742-4744.
74. T. Codd, M.-W. Chen, M. Roudjane, J. F. Stanton and T. A. Miller, *J. Chem. Phys.*, 2015, **142**, 184305.
75. M. C. Babin, J. A. DeVine, M. DeWitt, J. F. Stanton and D. M. Neumark, *J. Phys. Chem. Lett.*, 2020, **11**, 395-400.
76. K. Sharma, T. A. Miller and J. F. Stanton, *Int. Rev. Phys. Chem.*, 2021, **40**, 165-298.
77. C. Zhang, Benjamin L. Augenbraun, Z. D. Lasner, N. B. Vilas, J. M. Doyle and L. Cheng, *J. Chem. Phys.*, 2021, **155**, 091101.
78. M. Li and J. A. Coxon, *J. Chem. Phys.*, 1995, **102**, 2663-2674.
79. A. C. Paul, M. A. Reza and J. Liu, *J. Mol. Spectrosc.*, 2016, **330**, 142-146.
80. R. A. Y. Jr. and D. R. Yarkony, *J. Chem. Phys.*, 2006, **125**, 234301.
81. J. J. Dillon and D. R. Yarkony, *J. Chem. Phys.*, 2009, **130**, 154312-154312.
82. J. J. Dillon and D. R. Yarkony, *J. Chem. Phys.*, 2009, **131**, 134303-134303.
83. Y. Shen and D. R. Yarkony, *J. Phys. Chem. Lett.*, 2020, **11**, 7245-7252.
84. Y. Shen and D. R. Yarkony, *J. Phys. Chem. A*, 2020, **124**, 4539-4548.
85. Y. Shen and D. R. Yarkony, *J. Phys. Chem. A*, 2022, **126**, 61-67.
86. M. Li and J. A. Coxon, *J. Chem. Phys.*, 1992, **97**, 8961-8969.
87. H. L. Dai and R. W. Field, eds., *Molecular Dynamics and Spectroscopy by Stimulated Emission Pumping*, World Scientific, Singapore, 1995.
88. C. J. Stein, V. von Burg and M. Reiher, *J. Chem. Theory Comput.*, 2016, **12**, 3764-3773.
89. J. W. Park, R. Al-Saadon, M. K. MacLeod, T. Shiozaki and B. Vlasisavljevich, *Chem. Rev.*, 2020, **120**, 5878-5909.
90. K. Sharma, T. A. Miller, A. C. Paul and J. Liu, presented in part at the the 74th International Symposium on Molecular Spectroscopy, Urbana-Champaign, IL, FF06, 2019.
91. L. Baum, N. B. Vilas, C. Hallas, B. L. Augenbraun, S. Raval, D. Mitra and J. M. Doyle, *Phys. Rev. A*, 2021, **103**, 043111.
92. D. G. Melnik, J. Liu, M.-W. Chen, T. A. Miller and R. F. Curl, *J. Chem. Phys.*, 2011, **135**, 094310.
93. J. Liu, M.-W. Chen, D. Melnik, J. T. Yi and T. A. Miller, *J. Chem. Phys.*, 2009, **130**, 074302.
94. J. Liu, M.-W. Chen, D. Melnik, T. A. Miller, Y. Endo and E. Hirota, *J. Chem. Phys.*, 2009, **130**, 074303.